



OPEN Design and control of a permanent magnet-based robotic system for navigating tetherless magnetic devices in viscous environments

Zhengya Zhang^{1,5}, Anke Klingner², Sarthak Misra^{1,3} & Islam S. M. Khalil⁴✉

Tetherless magnetic devices (TMDs) that are driven using external stimuli have potential applications in minimally invasive surgery. The magnetic field produced by electromagnet- and permanent magnet-based robotic systems is a viable option as an external stimulus to enable the motion of a TMD in viscous and viscoelastic media. In order to realize the navigation of TMDs in fluidic environments, we design a permanent magnet-based robotic system with an open configuration using two synchronized rotating magnetic dipoles to generate time-varying rotating magnetic fields. These fields are used to apply torque on a TMD in low-Reynolds-number flow regimes. The configuration of the system is vertically symmetric, allowing permanent magnets to exert relatively uniform magnetic fields within the center of the workspace. We derive the configuration-to-pose kinematics and the pose-to-field mapping of the system. Such derivation is the basis for realizing the motion control of TMDs in three-dimensional space. The kinematic system holds one translational degree of freedom (DOF) and three rotational DOFs, allowing it to control the pose of actuator magnets with four DOFs. The nonlinear inverse kinematic problem is solved using an optimization algorithm. The experimental results of this level of control demonstrate that the mean absolute error and the maximum tracking error of three-dimensional motion control are 1.18 mm and 2.64 mm, respectively. This paper tackles the challenge of generating and controlling synchronized rotating magnetic fields to actuate and navigate TMDs. Commonly, this involves collaboratively manipulating two permanent magnets by attaching each to the end-effector of an industrial robot. This paper proposes a novel approach: robotically manipulating two permanent magnets through a symmetric configuration constrained by a connecting plate. This method simplifies the manipulation of rotating magnetic fields, thereby aiding the simplification of TMD motion control strategies. Future research will improve the design of this robotic system to offer more degrees of freedom, thus achieving greater flexibility in TMD motion control.

Keywords Rotating field, Synchronization, Untethered, Permanent magnet, Motion control, Kinematics-analysis, Tetherless magnetic device

Small-scale tetherless magnetic devices (TMDs) have the potential to improve minimally invasive medicine by precision surgery due to its dexterity¹, allowing them to access regions inaccessible by tethered surgical devices. With these merits, small-scale TMDs have attracted significant attention of being utilized in biomedical applications such as targeted drug delivery^{2,3}, nanotechnology^{4,5}, microfluidic^{6,7} and biomedical^{8,9} applications. One of the challenges in these applications is the precise TMD motion control along a prescribed trajectory^{10–12}. The vast majority of TMD motion control is achieved by using electromagnet-based robotic systems^{13–16}. Despite the merit of high controllability of generated uniform magnetic field (including orientation and strength control) by changing the coil current, and the ability to turn-off the magnetic field completely^{17–19}, these systems have some shortcomings, such as the difficulty of scaling up to the size of in vivo application due to the restriction of

¹Department of Biomaterials & Biomedical Technology, University of Groningen and University Medical Center Groningen, Groningen 9713 AV, The Netherlands. ²Department of Physics, The German University in Cairo, Cairo, Egypt. ³Department of Biomechanical Engineering, Faculty of Engineering Technology, University of Twente, Enschede 7500 AE, The Netherlands. ⁴Robotics and Mechatronics Research Group, Faculty of Electrical Engineering, Mathematics and Computer Science, University of Twente, Enschede 7500 AE, The Netherlands. ⁵Oujiang Laboratory (Zhejiang Lab for Regenerative Medicine, Vision and Brain Health), Wenzhou 325035, China. ✉email: i.s.m.khalil@utwente.nl

the projection distance of the field gradient, and heat emission problem due to the low efficiency of electric-to-magnetic conversion caused by the electromagnetic coils²⁰. In contrast to electromagnet-based robotic system, permanent magnet-based robotic systems can generate stronger magnetic field²¹, and have no heat emission problem. In particular, those with open configurations can be scaled up to the size of in vivo applications²². Consequently, permanent magnet-based robotic systems are becoming increasingly popular.

Depending on how a TMD is propelled, permanent magnet-based robotic systems can be classified based on the applied driving mode: (1) Torque-driven mode which serves the magnetic torque as the main form of actuation and propels a TMD (e.g., a helical microrobot) by rotating it. (2) Force-driven mode which serves magnetic force (i.e., the force due to magnetic gradient) as the main form of actuation and propels TMD by pulling it. (3) Torque-force-driven mode which serves either one of them (magnetic torque and force) or both of them as effective forms of actuation and to propel a TMD by rotating it or pulling it or both. Furthermore, permanent magnet-based robotic systems in each mode can be generalized into three categories based on the number of actuator magnets: (1) Using one actuator magnet. (2) Using two actuator magnets. (3) Using an array of actuator magnets.

The permanent magnet-based robotic systems in torque-driven mode rotate actuator magnets to generate a rotating magnetic field, resulting in a magnetic torque, as the main source of actuation, exerted on TMDs. With using one actuator magnet, Mahoney et al. have proposed a method to control the magnetic field at a point in space to be rotated about any desired axis with a constant frequency, thus the TMD motion is controlled by aligning the TMD's dipole moment with the applied magnetic field²³. Nelson et al. have provided a solution to generate two independent rotating magnetic fields with any desired field-rotation axes at any two points, allowing it for the independent motion control of two TMDs²⁴. Despite the controllability of the field-rotation axis, such systems may produce unnecessary magnetic force which creates a tendency for a TMD to move toward the actuator magnet. This unnecessary magnetic force can be reduced by increasing the distance between the TMD and the actuator magnet, yet the applied magnetic torque on the TMD is inevitably weakened. To overcome this undesired behavior, Mahoney et al. have presented a strategy to substantially reduce the magnetic force while maximizing the magnetic torque, by limiting the absolute upper boundary on the magnitude of maximum magnetic force for any orientation of TMD dipole moment²⁵. This strategy can diminish the magnetic force yet not eliminate it. With using two actuator magnets, Hosney et al. have designed a robotic system by rotating the two actuator magnets synchronously for the wireless motion control of a helical microrobot, which stabilizes the motion of the microrobot by eliminating the magnetic field gradient within the workspace of the microrobot and develops gravity compensation technology by manipulating the angular speed and motion direction of the microrobot²⁶. With using an array of actuator magnets, Zhang et al. have implemented a method of arranging the rotational actuator magnets circumferentially to generate a rotating magnetic field in the center area of the circle and obtain a synchronous reversing magnetic field with constant strength²⁷. Qiu et al. have developed a robotic system incorporating four rotary actuator magnets, which can generate a rotating magnetic field with the orientation of the field-rotation axis being arbitrary in a plane²⁸. Although these systems using an array of actuator magnets can generate rotating magnetic fields without the translational movement of actuator magnets, the number of DOFs of these robotic systems to control the magnetic field is potentially restricted.

The permanent magnet-based robotic systems in force-driven mode generate a magnetic gradient field, resulting in a magnetic force, as the main source of actuation, exerted on TMDs. With using one actuator magnet, Khalil et al. have demonstrated a robotic system that attaches the actuator magnet to the end-effector of a robotic arm, achieving the kinematic control of paramagnetic microparticles in 3-D space with the manipulation of the exerted field gradient on the dipole of the microparticles²⁹. Mahoney et al. have first demonstrated a 5-DOF manipulation of an untethered magnetic capsule by a 6-DOF robotic manipulator with the feedback of only 3-DOF capsule position³⁰. Magnetic force are utilized to manage the total force (the sum of magnetic force, gravitational force, and buoyancy force) applied on the capsule. With using two actuator magnets, Shapiro et al. have demonstrated the capability of a robotic system consisted of an arrangement of two permanent magnets to create magnetic force, and eventually to push therapeutic nanoparticles³¹. Amokrane et al. have optimized a robotic system to produce a maximum push-pull force on magnetic microparticles by manipulating magnetic field gradient, enabling the navigation of microparticles in cortical microvasculature network³². With using an array of actuator magnets, Abbas et al. have reported a robotic system with a magnetic unit being attached to the end-effector of a robotic arm such that the magnetic unit consists of four actuator magnets, demonstrating the steerability to push and pull the magnetic microparticles in viscous fluids³³. Son et al. have presented a robotic system that can create a strong magnetic force trap enabling a cylindrical millirobot to penetrate continuously into soft tissue. The penetration motion is assisted by the induced magnetic torque which directs the orientation of the millirobot to the center of the array of actuator magnets³⁴. In comparison to the systems in torque-driven mode, those in force-driven mode at the same level require more energy consumption in the propulsion of TMDs in fluids, making the systems in force-driven mode more suitable in use for the scenarios of driving small-scale TMDs when requiring to limit the size of actuator magnets.

The permanent magnet-based robotic systems in torque-force-driven mode generate a rotating magnetic field and gradient field, resulting in a magnetic torque and force, as the main sources of actuation simultaneously, exerted on TMDs. These systems can be selectively switched to those in torque-driven mode or those in force-driven mode according to the specific application, making them have extraordinary versatility. With using one actuator magnet, Mahoney et al. have proposed a method to convert the magnetic force into a lateral force by manipulating the actuator magnet to be rotated with a specific trajectory. Such an operation can make a TMD be simultaneously pushed and rolled on a surface, inducing potentially enhanced rolling motion (higher rolling velocity) or it may be used for the scenarios of levitating device³⁵. This method relies on the specific rotation control of the actuator magnet. With using two actuator magnets, Hosney et al. have introduced a strategy of combining the propulsion force converted from the magnetic torque and the magnetic force, which is proved to

decrease the drilling time of blood clots³⁶. Pittiglio et al. have developed a robotic system using two independent serial manipulators, which can generate a magnetic field with a high degree of manipulability by controlling the pose of two actuator magnets collaboratively, enabling the system to work in torque-force-driven mode suitably³⁷. With using an array of actuator magnets, Ryan et al. have built a robotic system to create fields and field gradients in any direction in three-dimensional (3-D) path-following tasks, and shown that this system is able to implement 1-D and 2-D motion control via rolling as well as 3-D motion control via gradient pulling³⁸. The disadvantage of this system is that the size of the workspace is severely restricted unless extremely large size actuator magnets are utilized³⁹.

In this paper, we focus on the permanent magnet-based robotic systems in torque-driven mode. Our system has an open configuration without using commercial robotic arms. The system holds one translational DOF and three rotational DOFs, enabling it to control the pose of two actuator magnets collaboratively with four DOFs. Further, the system is arranged with a vertically symmetric configuration to exert relatively uniform magnetic fields within the center of the workspace. This symmetric configuration is physically constrained through a connecting plate, which simplifies the yawing motion control of the field-rotation axis within the center region of the workspace by only driving one robotic joint, as a result, leading to an ease of yawing motion control of TMDs. Besides, the forward (from joint space variables to the orientation of field-rotation axis) and inverse kinematics (from desired orientation of field-rotation axis to desired joint space variables) of the system is analyzed, which serves as a basis of implementing TMD motion control. Our system is verified to have the ability of achieving TMD motion control in torque-driven mode. The remainder of the paper is organized as follows: “[Magnetic-based robotic system](#)” section provides the forward and inverse kinematic analysis of the magnet-based robotic system. “[Orienting field-rotation axis](#)” section analyzes the possible unreachable zone of the field-rotation axis at the central point of the workspace. “[Characterization of the magnetic field](#)” section investigates the magnetic field strength and field gradient within the workspace. “[Closed-loop motion control](#)” section validates the ability of implementing 3-D closed-loop motion control of TMDs conducted in an agar-gel phantom.

Magnetic-based robotic system

We consider a time-varying rotating magnetic field produced by the superposition of the contributions of multiple dipole sources. These dipole sources are fixed in three-dimensional space by a robotic configuration and exert a controlled magnetic torque on a TMD in low Reynolds (Re) numbers.

Magnetic actuation using multiple magnetic source

The magnetic field generated by multiple permanent magnets is characterized by the configuration-to-pose kinematics and the pose-to-field mapping. If a translation and rotation of multiple permanent magnets (with magnetic moment M_i for $i = 1, \dots, k$) using a robotic configuration would result in a superimposed magnetic field ($B(\mathbf{p})$), then the magnitude and direction of the magnetic field at position \mathbf{p} are completely characterized by the joint space variables $\mathbf{q} \in \mathbb{R}^n$. The configuration-to-pose kinematics of such a robotic configuration is given by

$$\{\mathbf{R}_i, \mathbf{x}_i\} = \mathcal{F}(\mathbf{q}), \quad \text{for } i = 1, \dots, k, \quad (1)$$

where \mathbf{R}_i and \mathbf{x}_i characterize the rotation and translation of the i th magnetic source using the forward kinematic mapping $\mathcal{F} : \mathbb{R}^n \rightarrow \{\mathbb{R}^3, SO(3)\}$, respectively. We can compute the magnetic field produced by each magnetic moment (M_i) in the global frame of reference $\{\mathcal{W}\}$ as follows:

$$\mathbf{B}(\mathbf{p}) = \sum_{i=1}^k (\mathbf{B}(\mathbf{x}_i, M_i) |_{\mathcal{W}}), \quad (2)$$

where $\mathbf{B}(\mathbf{x}_i, M_i) |_{\mathcal{W}}$ is the magnetic field due to the i th magnetic source with respect to the global frame of reference. Further, the magnetic field vector of $\mathbf{B}(\mathbf{x}_i, M_i) |_{\mathcal{W}}$ in Eq. (2) can be calculated by

$$\left[\mathbf{B}(\mathbf{x}_i, M_i) |_{\mathcal{W}} \right]_0 = {}^{\mathcal{W}}T_{\mathcal{E}_i} \left[\mathbf{B}(\mathbf{x}_i, M_i) |_{\mathcal{E}_i} \right], \quad (3)$$

where ${}^{\mathcal{W}}T_{\mathcal{E}_i}$ is the homogeneous transformation between the global frame of reference and the i th frame of reference of the magnetic source $\{\mathcal{E}_i\}$, as shown in Fig. 1. Further, $\mathbf{B}(\mathbf{x}_i, M_i) |_{\mathcal{E}_i}$ is the magnetic field due to the i th magnetic source in the local frame $\{\mathcal{E}_i\}$. The properties of the magnetic field $\mathbf{B}(\mathbf{p})$ is completely characterized by the pose of each magnetic moment (M_i) and can be manipulated using the joint space variables (\mathbf{q}).

Figure 1 shows the magnetic field produced by two identical magnetic dipole sources. For $k = 1$ and away from the region between the magnetic dipole sources, the magnitude of the magnetic field decreases approximately as the inverse cube of the distance $|\mathbf{p} - \mathbf{x}_i|$. The magnitude of the field scales approximately as the sum of the inverse cube of $|\mathbf{p} - \mathbf{x}_i|$ when two dipole sources are incorporated. Therefore, it is desirable to consider the enclosed region between the two dipole sources in order to create larger field strength than any other locations away from this region. For a small enough workspace (around position \mathbf{p}), it is possible to create a relation between the magnitude of the field and the distance to the dipole sources by placing a position constraint on the dipole sources. In such situation, the orientation of magnetic moment (M_i) can be controlled using a robotic configuration to manipulate the magnetic field at the position \mathbf{p} . At this point, the relationship

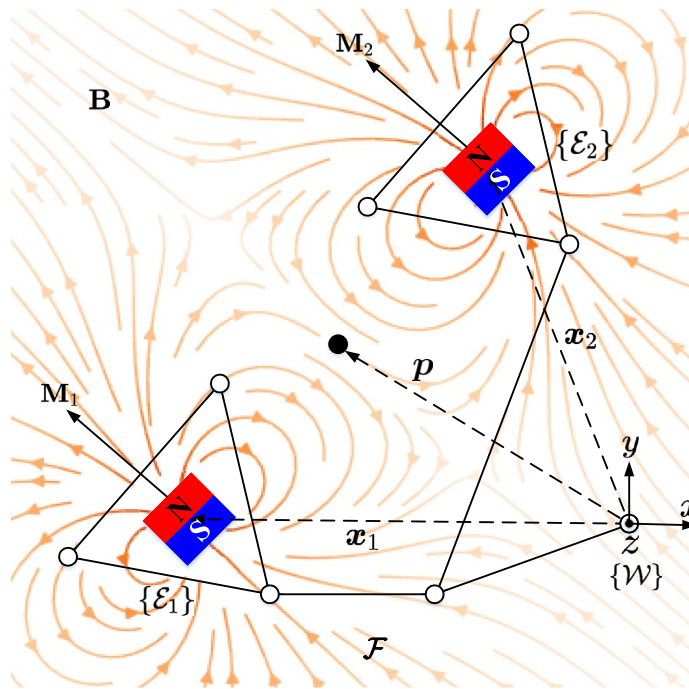


Fig. 1. The magnetic field at a point (p) is characterized by the configuration-to-pose kinematics (\mathcal{F}), and the pose-to-field mapping (\mathcal{B}) under the global frame of reference $\{\mathcal{W}\}$. Additionally the i th magnetic source is arranged a local frame of reference $\{\mathcal{E}_i\}$.

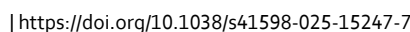
between the unit vector of field-rotation axis ($\hat{\omega}$, refer to the rotation axis of magnetic field $\mathcal{B}(p)$) and the unit vector of dipole-rotation axis ($\hat{\Omega}$, refer to the rotation axis of magnetic moment M_i) can be characterized by the configuration of the permanent-magnet robotic system, as shown in Fig. 2.

Robotic configuration

Superimposing the magnetic field of multiple magnetic sources can generate greater and uniform field within the enclosed region between the permanent magnets. Translating and rotating these magnetic sources can be used for actuation. Therefore, we need to control the pose of the magnetic sources by robotically moving a robotic configuration in order to obtain the desired field-rotation axis for actuation at p . Since we are considering rotating magnetic field for actuation, the magnetic dipole of the i th source can be continuously rotated in synchrony with an angle θ_s ($\theta_s = \Omega t$ such that Ω is the angular velocity of two synchronized rotating dipoles) about the i th dipole-rotation axis Ω . The orientation of these axes of rotation is completely characterized using the forward kinematics (\mathcal{F}).

To control the dipole-rotation axis Ω , a number of joints must be independently controlled. Here, we consider a translational base frame $\{\mathcal{A}\}$ supporting four actuated rotational joints. The pure translation of frame $\{\mathcal{A}\}$ with respect to the global frame of reference is characterized by the joint space variable q_1 , which enables the superimposed field to be translated without affecting its spatial derivatives. The first and second rotational joints are orthogonally arranged to rotate frame $\{\mathcal{B}\}$ and $\{\mathcal{C}\}$ about the z_2 - and x_3 -axes respectively, as shown in Fig. 2a. The rotation of frame $\{\mathcal{B}\}$ with respect to frame $\{\mathcal{A}\}$ and the rotation of frame $\{\mathcal{C}\}$ with respect to frame $\{\mathcal{B}\}$ are characterized by the joint space variable q_2 and q_3 , which enables control of the yawing and pitching motion of the field-rotation axis at p , respectively. Frame $\{\mathcal{C}\}$ supports two symmetrically placed actuated rotational joints aligned to rotate frame $\{\mathcal{D}_1\}$ and $\{\mathcal{D}_2\}$ about the z_4 - and z_5 -axes, respectively. The rotation of frame $\{\mathcal{D}_i\}$ with respect to frame $\{\mathcal{C}\}$ is characterized by the joint space variable q_4 , which also enables the control of yawing motion of the field-rotation axis at p . This allows us to have multiple control options (manipulating q_2 or q_4 or both of them) when to plan a yawing motion of field-rotation axis at p , and thus it improves the flexibility of our system. These joints are equally spaced with respect to the z -axis of the global frame of reference. Frame $\{\mathcal{T}_i\}$ is defined as the frame of reference of the i th permanent magnet, two magnetic sources rotate about the σ^i -axis of frame $\{\mathcal{T}_i\}$ such that their magnetic moment is orthogonal to these vectors. Further, frame $\{\mathcal{T}_i\}$ is only rigidly translational with respect to frame $\{\mathcal{D}_i\}$. In addition, the rotation of i th permanent magnet is characterized in frame $\{\mathcal{E}_i\}$ such that frame $\{\mathcal{E}_i\}$ is only rotational with respect to frame $\{\mathcal{T}_i\}$. The origin of $\{\mathcal{T}_i\}$ and that of frame $\{\mathcal{E}_i\}$ are overlapping and the v^i -axis of frame $\{\mathcal{E}_i\}$ and the σ^i -axis of frame $\{\mathcal{T}_i\}$ are coincident.

The configuration of the permanent-magnet robotic system is shown in Fig. 2a, it indicates the links and joints with the corresponding frames. The vector $\mathbf{q} \in \mathbb{R}^{4 \times 1}$ is constructed with independent joint space variables such that $\mathbf{q} = [q_1, q_2, q_3, q_4]^T$. Note that q_1 in \mathbf{q} refers to a translational motion, and q_2, q_3 and q_4 in \mathbf{q} refer to rotational motions. Besides the links and joints, Fig. 2b shows the permanent-magnet robotic system as well as



nature portfolio

where ${}^{\mathcal{W}}\mathbf{T}_{\mathcal{D}_i}$ is the homogeneous transformation matrix between the frame $\{\mathcal{D}_i\}$ and the global frame of reference. In Eq. (4), ${}^{\mathcal{W}}\mathbf{T}_{\mathcal{A}}$ is the homogeneous transformation matrix between frame $\{\mathcal{A}\}$ and the global frame of reference, which is given by

where \mathbf{I} is the unit matrix and $\mathbf{x}_A^{\mathcal{W}}$ is the translation vector of the origin of frame $\{\mathcal{A}\}$ in the global frame of reference. Further, $\mathbf{x}_A^{\mathcal{W}}$ is given by

The translation of the origin of frame $\{\mathcal{A}\}$ in the global frame of reference enables control of the translational motion of the superimposed field in the y -axis direction. Further, this translation partially determines the reachable zone of field-rotation axis at \mathbf{p} . In Eq. (4), ${}^{\mathcal{A}}\mathbf{T}_{\mathcal{B}}$ is the homogeneous transformation matrix between frame $\{\mathcal{B}\}$ and $\{\mathcal{A}\}$, which is given by

where ${}^A\mathbf{R}_B$ is the rotation matrix between frame $\{B\}$ with respect to $\{A\}$ and $\mathbf{x}_B^A = [0 \quad 0 \quad d_z^2]^T$ is the translation vector of the origin of frame $\{B\}$ in the frame $\{A\}$. Further, d_z^2 is a constant determined by mechanical dimensions of the system and $d_z^2 = l_2$. In Eq. (7), ${}^A\mathbf{R}_B$ is given by

$${}^A\mathbf{R}_B = \begin{bmatrix} \cos(q_2) & -\sin(q_2) & 0 \\ \sin(q_2) & \cos(q_2) & 0 \\ 0 & 0 & 1 \end{bmatrix}. \quad (8)$$

The rotation of frame $\{\mathcal{B}\}$ with respect to frame $\{\mathcal{A}\}$ enables control of the yawing motion of the field-rotation axis at \mathbf{p} . This yawing motion is important for the steering of TMDs. In Eq. (4), ${}^{\mathcal{B}}\mathbf{T}_{\mathcal{C}}$ is the homogeneous transformation matrix between frame $\{\mathcal{C}\}$ and $\{\mathcal{B}\}$.

$${}^{\mathcal{B}}\mathbf{T}_{\mathcal{C}} = \begin{bmatrix} {}^{\mathcal{B}}\mathbf{R}_{\mathcal{C}} & \mathbf{x}_{\mathcal{C}}^{\mathcal{B}} \\ \mathbf{0}_{1 \times 3} & 1 \end{bmatrix}, \quad (9)$$

where ${}^{\mathcal{B}}\mathbf{R}_{\mathcal{C}}$ is the rotation matrix of frame $\{\mathcal{C}\}$ with respect to frame $\{\mathcal{B}\}$ and $\mathbf{x}_{\mathcal{C}}^{\mathcal{B}} = [0 \ 0 \ d_z^3]^T$ is the translation vector of the origin of frame $\{\mathcal{C}\}$ in the frame $\{\mathcal{B}\}$. Further, d_z^3 is a constant determined by mechanical dimensions of the system and $d_z^3 = l_3$. In Eq. (9), ${}^{\mathcal{B}}\mathbf{R}_{\mathcal{C}}$ is given by

$${}^{\mathcal{B}}\mathbf{R}_{\mathcal{C}} = \begin{bmatrix} 1 & 0 & 0 \\ 0 & \cos(q_3) & -\sin(q_3) \\ 0 & \sin(q_3) & \cos(q_3) \end{bmatrix}. \quad (10)$$

The rotation of frame $\{\mathcal{C}\}$ with respect to frame $\{\mathcal{B}\}$ enables control of the pitching motion of the field-rotation axis at \mathbf{p} . This pitching motion is important for TMDs to swim upward or downward and follow a 3-D prescribed trajectory. In Eq. (4), ${}^{\mathcal{C}}\mathbf{T}_{\mathcal{D}_i}$ is the homogeneous transformation matrix between frame $\{\mathcal{D}_i\}$ and $\{\mathcal{C}\}$, which is given by

$${}^{\mathcal{C}}\mathbf{T}_{\mathcal{D}_i} = \begin{bmatrix} {}^{\mathcal{C}}\mathbf{R}_{\mathcal{D}_i} & \mathbf{x}_{\mathcal{D}_i}^{\mathcal{C}} \\ \mathbf{0}_{1 \times 3} & 1 \end{bmatrix}, \quad (11)$$

where ${}^{\mathcal{C}}\mathbf{R}_{\mathcal{D}_i}$ is the rotation matrix of frame $\{\mathcal{D}_i\}$ with respect to frame $\{\mathcal{C}\}$ and $\mathbf{x}_{\mathcal{D}_i}^{\mathcal{C}} = [d_x^4 \ d_y^4 \ d_z^4]^T$ is the translation vector of the origin of frame $\{\mathcal{D}_i\}$ in the frame $\{\mathcal{C}\}$. Further, d_x^4 , d_y^4 and d_z^4 are constants determined by mechanical dimensions of the system. For $i = 1$, $d_x^4 = l_5$, $d_y^4 = -l_6$ and $d_z^4 = l_4$. For $i = 2$, $d_x^4 = -l_5$, $d_y^4 = l_6$ and $d_z^4 = l_4$. In Eq. (11), ${}^{\mathcal{C}}\mathbf{R}_{\mathcal{D}_i}$ is given by

$${}^{\mathcal{C}}\mathbf{R}_{\mathcal{D}_i} = \begin{bmatrix} \cos(q_4) & -\sin(q_4) & 0 \\ \sin(q_4) & \cos(q_4) & 0 \\ 0 & 0 & 1 \end{bmatrix}. \quad (12)$$

Like the function of rotation matrix ${}^{\mathcal{A}}\mathbf{R}_{\mathcal{B}}$, the rotation of frame $\{\mathcal{D}_i\}$ with respect to frame $\{\mathcal{C}\}$ also enables the control of yawing motion of the field-rotation axis at \mathbf{p} . However, this redundancy allows multiple options to control the yawing motion of field-rotation axis at \mathbf{p} , and it expands the reachable zone of field-rotation axis at \mathbf{p} . The configuration-to-pose kinematics of our robotic configuration characterizes the i th dipole-rotation axis in terms of the joint space variables, such that

$$\begin{bmatrix} \hat{\Omega} \\ 0 \end{bmatrix} = {}^{\mathcal{W}}\mathbf{T}_{\mathcal{D}_i} \begin{bmatrix} \mathbf{o}_{\mathcal{D}_i}^i \\ 0 \end{bmatrix} = {}^{\mathcal{W}}\mathbf{T}_{\mathcal{T}_i} \begin{bmatrix} \mathbf{o}^i \\ 0 \end{bmatrix} = {}^{\mathcal{W}}\mathbf{T}_{\mathcal{E}_i} \begin{bmatrix} \mathbf{v}^i \\ 0 \end{bmatrix}, \quad (13)$$

where $\mathbf{o}_{\mathcal{D}_i}^i$ characterizes the rotation axis of i th magnetic source in the frame $\{\mathcal{D}_i\}$. In configuration-to-pose kinematics, ${}^{\mathcal{W}}\mathbf{T}_{\mathcal{T}_i}$ is the homogeneous transformation matrix between the frame $\{\mathcal{T}_i\}$ and the global frame of reference, which is given by

$${}^{\mathcal{W}}\mathbf{T}_{\mathcal{T}_i} = {}^{\mathcal{W}}\mathbf{T}_{\mathcal{D}_i} {}^{\mathcal{D}_i}\mathbf{T}_{\mathcal{T}_i}. \quad (14)$$

Further, ${}^{\mathcal{D}_i}\mathbf{T}_{\mathcal{T}_i}$ is the homogeneous transformation matrix between the frame $\{\mathcal{T}_i\}$ and $\{\mathcal{D}_i\}$, which is given by

$${}^{\mathcal{D}_i}\mathbf{T}_{\mathcal{T}_i} = \begin{bmatrix} \mathbf{I} & \mathbf{x}_{\mathcal{T}_i}^{\mathcal{D}_i} \\ \mathbf{0}_{1 \times 3} & 1 \end{bmatrix}, \quad (15)$$

where $\mathbf{x}_{\mathcal{T}_i}^{\mathcal{D}_i} = [0 \ d_y^5 \ d_z^5]^T$ is the translation vector of the origin of frame $\{\mathcal{T}_i\}$ in frame $\{\mathcal{D}_i\}$. Further, d_y^5 and d_z^5 are constants determined by mechanical dimensions of the system. For $i = 1$, $d_y^5 = l_6$ and $d_z^5 = l_7$. For $i = 2$, $d_y^5 = -l_6$ and $d_z^5 = l_7$. Multiplying the solution for all transformation matrices, results in the overall homogeneous transformation matrix ${}^{\mathcal{W}}\mathbf{T}_{\mathcal{T}_i}$ which governs the relation between the vector of joint space variables \mathbf{q} and unit vector of dipole-rotation axis $\hat{\Omega}$.

Mapping dipole-rotation axis to field-rotation axis

The unit vector of field-rotation axis $\hat{\omega}$ at \mathbf{p} is defined to be perpendicular to the plane containing $\mathbf{B}(\mathbf{p})$, such that $\hat{\omega}^T \mathbf{B}(\mathbf{p}) = 0$ for all M_i . Replacing $\mathbf{B}(\mathbf{p})$ with Eq. (2) in this expression yields

$$\begin{bmatrix} \hat{\omega} \\ 0 \end{bmatrix}^T \sum_{i=1}^k \left(\begin{bmatrix} \mathbf{B}(\mathbf{x}_i, M_i) \\ 0 \end{bmatrix} | \mathbf{w} \right) = 0. \quad (16)$$

Substituting Eq. (3) into (16) yields

$$\begin{bmatrix} \hat{\omega} \\ 0 \end{bmatrix}^T \sum_{i=1}^k \left(w_{T_{\mathcal{E}_i}} \begin{bmatrix} B(\mathbf{x}_i, M_i) |_{\mathcal{E}_i} \\ 0 \end{bmatrix} \right) = 0, \quad (17)$$

such that,

$$w_{T_{\mathcal{E}_i}} = w_{T_{\mathcal{T}_i}} {}^{\mathcal{T}_i}T_{\mathcal{E}_i}, \quad (18)$$

where ${}^{\mathcal{T}_i}T_{\mathcal{E}_i}$ is the homogeneous transformation matrix between frame $\{\mathcal{E}_i\}$ and $\{\mathcal{T}_i\}$, which is given by

$${}^{\mathcal{T}_i}T_{\mathcal{E}_i} = \begin{bmatrix} {}^{\mathcal{T}_i}R_{\mathcal{E}_i} & \mathbf{0}^{3 \times 1} \\ \mathbf{0}^{1 \times 3} & 1 \end{bmatrix}, \quad (19)$$

where ${}^{\mathcal{T}_i}R_{\mathcal{E}_i}$ is the rotation matrix of frame $\{\mathcal{E}_i\}$ with respect to frame $\{\mathcal{T}_i\}$. Further, ${}^{\mathcal{T}_i}R_{\mathcal{E}_i}$ is given by

$${}^{\mathcal{T}_i}R_{\mathcal{E}_i} = \begin{bmatrix} \cos(\theta_s) & 0 & \sin(\theta_s) \\ 0 & 1 & 0 \\ -\sin(\theta_s) & 0 & \cos(\theta_s) \end{bmatrix}. \quad (20)$$

Note that θ_s is the synchronous rotation angle of the two rotating magnetic dipoles. The generated magnetic field due to i th magnetic source in the frame $\{\mathcal{E}_i\}$ can be rewritten as

$$B(\mathbf{x}_i, M_i) |_{\mathcal{E}_i} = (B_u^i \mathbf{u}^i + B_v^i \mathbf{v}^i + B_w^i \mathbf{w}^i), \quad \text{for } i = 1, 2, \quad (21)$$

where \mathbf{u}^i , \mathbf{v}^i and \mathbf{w}^i are the unit axis vector of frame $\{\mathcal{E}_i\}$. Further, B_u , B_v and B_w are magnitudes of the magnetic field along the direction of \mathbf{u}^i -, \mathbf{v}^i - and \mathbf{w}^i -axis in frame $\{\mathcal{E}_i\}$, respectively. Substituting Eq. (21) into Eq. (17) yields

$$\begin{bmatrix} \hat{\omega} \\ 0 \end{bmatrix}^T \sum_{i=1}^k w_{T_{\mathcal{E}_i}} \left(\begin{bmatrix} (B_u^i \mathbf{u}^i + B_w^i \mathbf{w}^i) \\ 0 \end{bmatrix} + B_v^i \begin{bmatrix} \mathbf{v}^i \\ 0 \end{bmatrix} \right) = 0. \quad (22)$$

Substituting Eq. (13) into expanded Equation (22) yields

$$\begin{bmatrix} \hat{\omega} \\ 0 \end{bmatrix}^T \sum_{i=1}^k \left(w_{T_{\mathcal{E}_i}} \begin{bmatrix} (B_u^i \mathbf{u}^i + B_w^i \mathbf{w}^i) \\ 0 \end{bmatrix} + B_v^i \begin{bmatrix} \hat{\Omega} \\ 0 \end{bmatrix} \right) = 0. \quad (23)$$

Hence the relationship between the unit vector of field-rotation axis $\hat{\omega}$, the unit vector of dipole-rotation axis $\hat{\Omega}$ and the vector of joint space variables \mathbf{q} at position \mathbf{p} is found.

Inverse kinematics

Given the desired unit vector of field-rotation axis $\hat{\omega}^d$, then the problem of solving inverse kinematics is converted to that of solving Eq. (23) with the orientation of the dipole moment of each magnetic source (M_i) varying synchronously and periodically in time. The algorithm flow of solving inverse solutions based on the desired field-rotation axis is presented in Algorithm I. The frame parameters required for the algorithm are demonstrated in Table 2 (see Appendix A) where the $l_1 = 0$ mm, $l_2 = 128$ mm, $l_3 = 60.6$ mm, $l_4 = 46$ mm, $l_5 = 175$ mm, $l_6 = 89$ mm and $l_7 = 119$ mm. In the algorithm, the increase and decrease of the value of joint space variable q_1 indicates the positive and negative linear motion of translational joint, respectively. Similarly, the increase and decrease of the value of joint space variable q_2 (q_3 or q_4) indicates the counterclockwise and clockwise rotation of that revolute joint, respectively. In particular, our permanent-magnet robotic system allows two consecutive clockwise or counterclockwise rotations of frame $\{\mathcal{B}\}$ with respect to frame $\{\mathcal{A}\}$, which is characterized by joint space variable q_2 ($q_2 \in [-720^\circ:720^\circ]$), enabling TMDs make two continuous clockwise or counterclockwise rotations.

Algorithm: Solving inverse kinematics based on desired unit vector of field-rotation axis $\hat{\omega}^d$ at a point

Input: Position \mathbf{p} , unit axis vector $\hat{\omega}^d$ and threshold δ_0
Output: Desired vector of joint variables \mathbf{q}^d

```

01:   $q_1 \in [-150:150], \quad q_2 \in [-720^\circ:720^\circ],$ 
       $q_3 \in [-90^\circ:90^\circ], \quad q_4 \in [-180^\circ:180^\circ],$ 
02:  Initialize the vector of joint variables  $\mathbf{q}$ 
03:   $\mathcal{H}_j(\mathbf{q}) \leftarrow \mathbf{p}$  and  $\hat{\omega}^d$ 
04:   $j = 1 : N$ 
05:     $\theta_s = (j/N) * 360^\circ$ 
06:     $\mathcal{F}(\mathbf{q}) \leftarrow \mathbf{q}$ 
07:     ${}^{\mathcal{W}}\mathbf{T}_{\mathcal{D}_i} \leftarrow \mathcal{F}(\mathbf{q})$ 
08:     ${}^{\mathcal{W}}\mathbf{T}_{\mathcal{T}_i} \leftarrow {}^{\mathcal{W}}\mathbf{T}_{\mathcal{D}_i} {}^{\mathcal{D}_i}\mathbf{T}_{\mathcal{T}_i}$ 
09:     ${}^{\mathcal{W}}\mathbf{T}_{\mathcal{E}_i} \leftarrow {}^{\mathcal{W}}\mathbf{T}_{\mathcal{T}_i} {}^{\mathcal{T}_i}\mathbf{T}_{\mathcal{E}_i}$ 
10:     ${}^{\mathcal{W}}\mathbf{T}_{\mathcal{E}_i}^{-1} \leftarrow {}^{\mathcal{W}}\mathbf{T}_{\mathcal{E}_i}$ 
11:     ${}^{\mathcal{E}_i}\mathbf{p} \leftarrow {}^{\mathcal{W}}\mathbf{T}_{\mathcal{E}_i}^{-1} \mathbf{p}$ 
12:     ${}^{\mathcal{E}_i}\mathbf{B}(\mathbf{p}) \leftarrow \mathbf{B}({}^{\mathcal{E}_i}\mathbf{p})$ 
13:     $[B_u^i \ B_v^i \ B_w^i] \leftarrow {}^{\mathcal{E}_i}\mathbf{B}(\mathbf{p})$ 
14:     $\mathcal{H}_j(\mathbf{q}) \leftarrow$  Equation (24)
15:    if  $\mathcal{H}_j(\mathbf{q}) \leq \delta_0$ 
16:       $\mathbf{q}^d = \mathbf{q}$ 
17:      break;
18:    end
19:  end
20:  Return  $\mathbf{q}^d$ 

```

Algorithm 1. Pseudocode for inverse kinematics.

To maintain the synchronous rotation of a TMD with the rotating magnetic field, the magnetic torque must balance the drag torque on the TMD. We allow two rotating actuator permanent magnets to be close to each other to generate greater magnetic torque than with a single rotating actuator permanent magnet. To precisely model the magnetic field in the workspace between two actuator permanent magnets, we use an exact magnetic model⁴⁰. With this model, the fitness function $\mathcal{H}_j(\mathbf{q})$ in Algorithm 1 is designed as

$$\mathcal{H}_j(\mathbf{q}) = \frac{180}{\pi} \arccos \left[\frac{(\hat{\omega}^d)^T \sum_{i=1}^k (\mathbf{B}(\mathbf{x}_i, \mathbf{M}_i) |_{\mathcal{W}})}{|\hat{\omega}^d| \left| \sum_{i=1}^k (\mathbf{B}(\mathbf{x}_i, \mathbf{M}_i) |_{\mathcal{W}}) \right|} \right] - 90. \quad (24)$$

The fitness function is optimized to approach 0 using Levenberg–Marquard (LM) algorithm. In Eq. (24), $\sum_{i=1}^k \mathbf{B}(\mathbf{x}_i, \mathbf{M}_i) |_{\mathcal{W}}$ can be calculated through

$$\left[\sum_{i=1}^k \mathbf{B}(\mathbf{x}_i, \mathbf{M}_i) |_{\mathcal{W}} \right]_0 = \sum_{i=1}^k {}^{\mathcal{W}}\mathbf{T}_{\mathcal{E}_i} [B_u^i \ B_v^i \ B_w^i \ 0]^T. \quad (25)$$

Referring to Algorithm 1, the desired vector of joint variables \mathbf{q}^d and desired unit vector of dipole-rotation axis $\hat{\omega}^d$ can be calculated based on the desired unit vector of field-rotation axis $\hat{\omega}^d$.

Control of a tetherless magnetic device

The TMD motion control scheme consists of motion direction control and motion speed control. The motion direction control of a TMD is implemented by manipulating TMD rotation axis such that the TMD rotation axis is directly determined by the field-rotation axis at TMD position. The motion speed control of a TMD is achieved by managing the actuation frequency of applied rotating magnetic field. We assume a TMD is actuated by an external rotating magnetic field with a constant rotation frequency, thus the TMD motion speed is expected to be constant. Then the motion control of the TMD is simplified to only control the motion direction of the TMD. Given a predefined trajectory (see Table 1), which is expressed mathematically as the parametric equation $x = f(t)$, $y = g(t)$, $z = h(t)$, we break it down into 17 waypoints. Point P_n is the n th representative waypoint. The necessary TMD motion direction $\hat{\mathbf{U}}$ at each waypoint P_n is found as

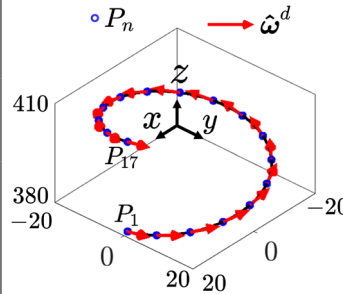
Predefined 3-D trajectory				Point p	P_1	P_2	P_3	P_4	P_5	P_6	P_7
				$\hat{\omega}^d$	$\begin{bmatrix} 0 \\ 0.981 \\ 0.194 \end{bmatrix}$	$\begin{bmatrix} 0.375 \\ 0.906 \\ 0.194 \end{bmatrix}$	$\begin{bmatrix} 0.694 \\ 0.694 \\ 0.194 \end{bmatrix}$	$\begin{bmatrix} 0.906 \\ 0.375 \\ 0.194 \end{bmatrix}$	$\begin{bmatrix} 0.981 \\ 0 \\ 0.194 \end{bmatrix}$	$\begin{bmatrix} 0.906 \\ -0.375 \\ 0.194 \end{bmatrix}$	$\begin{bmatrix} 0.694 \\ -0.694 \\ 0.194 \end{bmatrix}$
				$\hat{\Omega}^d$	$\begin{bmatrix} -0.023 \\ 0.989 \\ 0.147 \end{bmatrix}$	$\begin{bmatrix} -0.393 \\ 0.907 \\ 0.149 \end{bmatrix}$	$\begin{bmatrix} -0.706 \\ 0.693 \\ 0.148 \end{bmatrix}$	$\begin{bmatrix} -0.916 \\ 0.375 \\ 0.143 \end{bmatrix}$	$\begin{bmatrix} -0.991 \\ 0.001 \\ 0.134 \end{bmatrix}$	$\begin{bmatrix} -0.916 \\ -0.381 \\ 0.123 \end{bmatrix}$	$\begin{bmatrix} -0.695 \\ -0.709 \\ 0.117 \end{bmatrix}$
				q^d	$\begin{bmatrix} -0.134 \\ 3.729 \\ 8.459 \\ -2.353 \end{bmatrix}$	$\begin{bmatrix} 5.493 \\ 25.15 \\ 8.573 \\ -1.728 \end{bmatrix}$	$\begin{bmatrix} 10.34 \\ 46.48 \\ 8.530 \\ -0.933 \end{bmatrix}$	$\begin{bmatrix} 13.86 \\ 68.01 \\ 8.225 \\ -0.283 \end{bmatrix}$	$\begin{bmatrix} -15.30 \\ 89.99 \\ 7.679 \\ -0.026 \end{bmatrix}$	$\begin{bmatrix} 14.46 \\ 113.0 \\ 7.071 \\ -0.421 \end{bmatrix}$	$\begin{bmatrix} 11.47 \\ 137.0 \\ 6.704 \\ -1.405 \end{bmatrix}$
P_8	P_9	P_{10}	P_{11}	P_{12}	P_{13}	P_{14}	P_{15}	P_{16}	P_{17}		
$\begin{bmatrix} 0.375 \\ -0.906 \\ 0.194 \end{bmatrix}$	$\begin{bmatrix} 0 \\ -0.981 \\ 0.194 \end{bmatrix}$	$\begin{bmatrix} -0.375 \\ -0.906 \\ 0.194 \end{bmatrix}$	$\begin{bmatrix} -0.694 \\ -0.694 \\ 0.194 \end{bmatrix}$	$\begin{bmatrix} -0.906 \\ -0.375 \\ 0.194 \end{bmatrix}$	$\begin{bmatrix} -0.981 \\ 0 \\ 0.194 \end{bmatrix}$	$\begin{bmatrix} -0.906 \\ 0.375 \\ 0.194 \end{bmatrix}$	$\begin{bmatrix} -0.694 \\ 0.694 \\ 0.194 \end{bmatrix}$	$\begin{bmatrix} -0.375 \\ 0.906 \\ 0.194 \end{bmatrix}$	$\begin{bmatrix} 0 \\ 0.981 \\ 0.194 \end{bmatrix}$		
$\begin{bmatrix} -0.362 \\ -0.925 \\ 0.119 \end{bmatrix}$	$\begin{bmatrix} 0.0184 \\ -0.992 \\ 0.126 \end{bmatrix}$	$\begin{bmatrix} 0.392 \\ -0.911 \\ 0.131 \end{bmatrix}$	$\begin{bmatrix} 0.707 \\ -0.695 \\ 0.132 \end{bmatrix}$	$\begin{bmatrix} 0.918 \\ -0.376 \\ 0.126 \end{bmatrix}$	$\begin{bmatrix} 0.993 \\ 0 \\ 0.114 \end{bmatrix}$	$\begin{bmatrix} 0.920 \\ 0.381 \\ 0.0963 \end{bmatrix}$	$\begin{bmatrix} 0.698 \\ 0.711 \\ 0.0899 \end{bmatrix}$	$\begin{bmatrix} 0.367 \\ 0.925 \\ 0.094 \end{bmatrix}$	$\begin{bmatrix} -0.0133 \\ 0.994 \\ 0.104 \end{bmatrix}$		
$\begin{bmatrix} 6.355 \\ 160.9 \\ 6.838 \\ -2.265 \end{bmatrix}$	$\begin{bmatrix} 0.312 \\ 183.4 \\ 7.232 \\ -2.32 \end{bmatrix}$	$\begin{bmatrix} -5.377 \\ 205.0 \\ 7.535 \\ -1.718 \end{bmatrix}$	$\begin{bmatrix} -10.28 \\ 226.4 \\ 7.567 \\ -0.920 \end{bmatrix}$	$\begin{bmatrix} -13.84 \\ 248.0 \\ 7.219 \\ -0.274 \end{bmatrix}$	$\begin{bmatrix} -15.30 \\ 270.0 \\ 6.542 \\ -0.027 \end{bmatrix}$	$\begin{bmatrix} -14.46 \\ 292.9 \\ 5.526 \\ -0.398 \end{bmatrix}$	$\begin{bmatrix} -11.44 \\ 316.8 \\ 5.160 \\ -1.277 \end{bmatrix}$	$\begin{bmatrix} -6.386 \\ 340.4 \\ 5.396 \\ -2.043 \end{bmatrix}$	$\begin{bmatrix} -0.400 \\ 362.9 \\ 5.970 \\ -2.122 \end{bmatrix}$		

Table 1. Inverse solutions at separate points from a predefined 3-D spiral trajectory with calculating the desired field-rotation axis ($\hat{\omega}^d$), desired dipole-rotation axis ($\hat{\Omega}^d$) and desired vector of joint variables (q^d) at 17 representative waypoints.

$$\hat{U}(P_n) = \frac{\begin{bmatrix} \frac{dx}{dt} & \frac{dy}{dt} & \frac{dz}{dt} \end{bmatrix}^T}{\sqrt{(\frac{dx}{dt})^2 + (\frac{dy}{dt})^2 + (\frac{dz}{dt})^2}}. \quad (26)$$

Replacing the $\hat{\omega}^d$ with $\hat{U}(P_n)$ in Algorithm 1, we can acquire the desired vector of joint variables (q^d) at each waypoint, as shown in Table 1.

Orienting field-rotation axis

The challenge of aligning the field-rotation axis in diverse directions varies depending on the design of the robotic system and the constraints of joint space variables. Since the orientation of the field-rotation axis, as denoted by the unit vector of field-rotation axis, governs the motion direction of a TMD, it's imperative to analyze the difficulty level of orienting the field-rotation axis within its reachable orientation zone at the TMD's location. In this section, we'll presume the TMD is positioned at the central point of the workspace. The central point is defined as the middle point of line segment between two actuator magnets' centroids when the system is at its initial state. The initial system state refers to $q = 0^{4 \times 1}$. Subsequently, we'll evaluate the difficulty of aligning the field-rotation axis to a particular direction at this central point.

Yawing and pitching motion of field-rotation axis

The yawing and pitching motion of field-rotation axis plays an important role on the motion direction control of TMDs. Specifically, at the central point, we associate the yawing motion of the field-rotation axis with joint space variable q_2 , and the pitching motion with joint space variable q_3 .

Figure 3 shows the orientation of field-rotation axis changes along with q_2 and q_3 . The q_2 enables the yawing motion of the field-rotation axis at the central point, as shown in Fig. 3a. The unit vector of field-rotation axis rotates uniformly as q_2 varies at equal intervals over one revolution, which means the rotation of field-rotation axis is synchronized with the rotation of q_2 . Note that the unit vector of field-rotation axis at the case of $q_2 = 0^\circ$ is overlapped by that at the case of $q_2 = 360^\circ$. The q_3 enables the pitching motion of field-rotation axis, as shown in Fig. 3b. The unit vector of field-rotation axis rotates non-uniformly as q_3 varies at equal intervals from -90° to 90° , which means the rotation of field-rotation axis is not synchronized to the rotation of q_3 . Meanwhile, the rotational direction of the unit vector of field-rotation axis changes from clockwise ① to counterclockwise ②, and then back to clockwise ③.

Motion space of actuator magnets

The robotic joint space determines the motion space of actuator magnets, while the actuator magnets' motion space determines the field-rotation axis's reachable orientation zone at any point in the workspace. With revolute joints, the motion space of two actuator magnets is a hollow ellipsoid-like space and can be covered by an 800 mm \times 800 mm \times 500 mm cuboid, as shown in Fig. 4a. With all joints (revolute plus translational joints), the

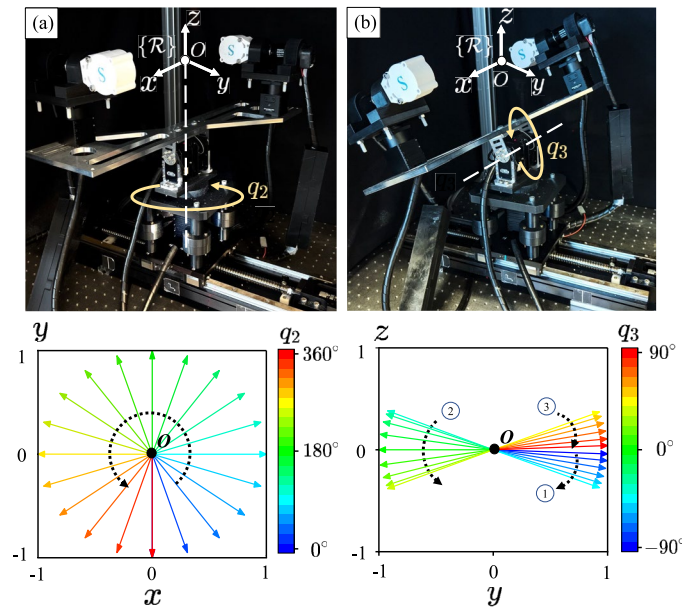


Fig. 3. Characterization of the yawing motion and pitching motion of the unit vector of field-rotation axis with respect to joint space variable q_2 and q_3 at the central point of the workspace in the frame $\{\mathcal{R}\}$. The arrows indicate the unit vectors of field-rotation axis. (a) The unit vector of field-rotation axis rotates counterclockwise in x - y plane as joint space variable q_2 varies from 0° to 360° . (b) The vector of field-rotation axis first rotates clockwise as indicated by ①, then rotates counterclockwise as indicated by ②, and finally rotates clockwise back as indicated by ③ in y - z plane as joint space variable q_3 varies from -90° to 90° . Please refer to the Segments S1 and S2 in [Supplementary Video](#) for a visual demonstration..

motion space of two actuator magnets is a cylinder-like space and can be covered by an $800 \text{ mm} \times 1000 \text{ mm} \times 500 \text{ mm}$ cuboid, as shown in Fig. 4b.

Difficulty level of orienting the field-rotation axis

In this part, we will analyze the difficulty level of orienting the field-rotation axis towards different directions at the central point of the workspace. We assume that the position of the central point with respect to frame $\{\mathcal{A}\}$ (see Fig. 2) is unchanged. That is to say, the central point follows the translational motion of frame $\{\mathcal{A}\}$ along y -axis. Thus, the translational motion of the frame $\{\mathcal{A}\}$, which is characterized by the joint space variable q_1 , does not affect the positions of actuator magnets (x_i) and the orientation of the dipole-rotation axis ($\hat{\Omega}$) in the frame $\{\mathcal{A}\}$. Therefore, the joint space variable q_1 does not influence the field-rotation axis at the central point since the field-rotation axis at any point in the workspace is purely a function of the actuator permanent magnets' positions (x_i) and dipole-rotation axis' orientation ($\hat{\Omega}$). Furthermore, to maximize the size of the workspace while maintaining a strong magnetic field strength, we set the joint space variable q_4 to 0. Thus, we design a new vector of joint space variables \mathbf{q}_n that does not contain the joint space variables q_1 and q_4 such that $\mathbf{q}_n = [q_2 \ q_3]^T$. Then we investigate the unreachable zone of the field-rotation axis at the central point by only considering robotic revolute joints. The matrix $\mathbf{J}_{\mathcal{F}}(\mathbf{q}_n) \in \mathbb{R}^{3 \times 2}$ is created to approximately map the small change ($\delta \mathbf{q}_n$) in the robotic joints to the small change ($\delta \hat{\omega}$) in the orientation of field-rotation axis, which is expressed by

$$\delta \hat{\omega} \approx \mathbf{J}_{\mathcal{F}}(\mathbf{q}_n) \delta \mathbf{q}_n. \quad (27)$$

Equation (27) can be inverted to generate the inverse mapping of desired change in the orientation of field-rotation axis to a desired change in the robotic joints using Moore–Penrose pseudoinverse,

$$\delta \mathbf{q}_n \approx \mathbf{J}_{\mathcal{F}}^\dagger(\mathbf{q}_n) \delta \hat{\omega}, \quad (28)$$

where the Moore–Penrose pseudoinverse $\mathbf{J}_{\mathcal{F}}^\dagger(\mathbf{q}_n)$ is the inverse mapping that minimizes $\|\mathbf{q}_n\|$ if the robotic system is over-actuated. The largest singular value of $\mathbf{J}_{\mathcal{F}}^\dagger(\mathbf{q}_n)$ serves as a measure of the most extreme scenario where a change in the unit vector of the field-rotation axis is approximately mapped to a magnitude change in the robotic joints⁴¹. If the largest singular value approaches infinity, the robotic system is close to experiencing a kinematic singularity.

To assess the system's capability to make a TMD ascend or descend at its central point, we measure the difficulty of executing the system as the field-rotation axis approaches the vertical direction at the central point. The orientation of the field-rotation axis at the central point is characterized by angles θ and φ . Specifically, the θ refers to the angle between the projection vector of the field-rotation axis and the positive x -axis, and the φ refers

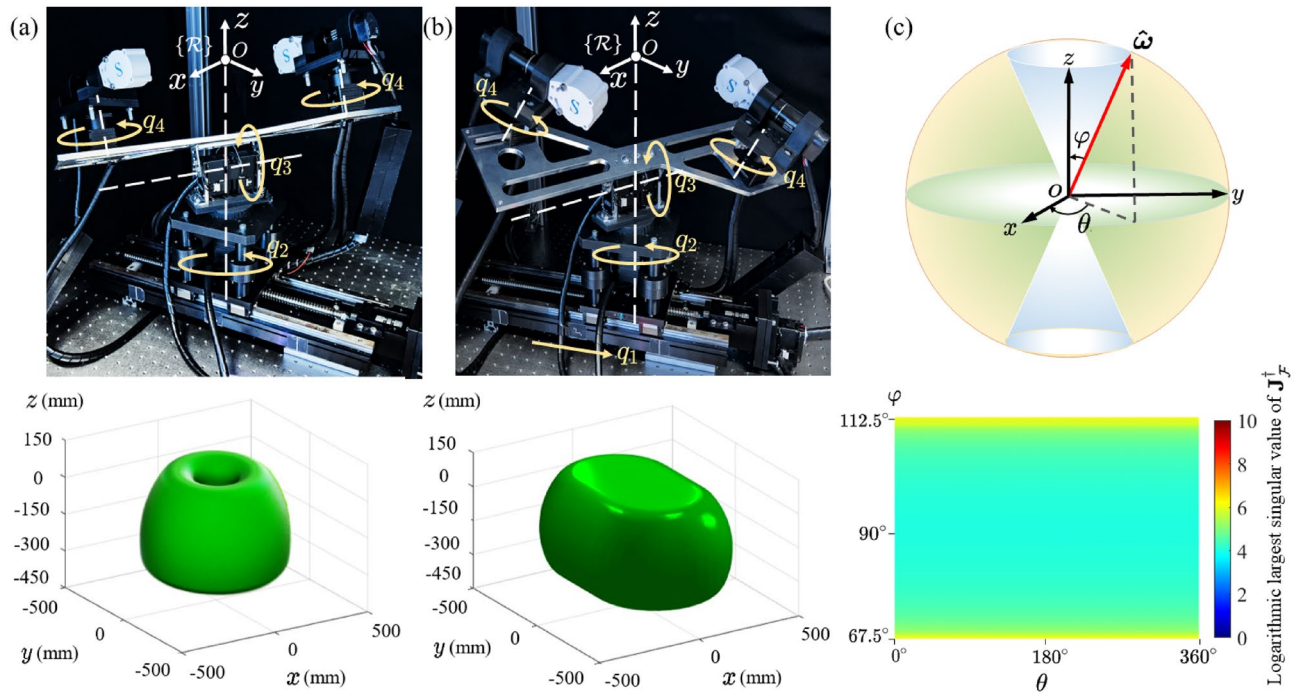


Fig. 4. Mapping the robotic joint space to the orientation of the field-rotation axis at the central point (O) of the workspace. (a) The motion space of actuator magnets relative to robotic revolute joints. (b) The motion space of actuator magnets relative to robotic revolute and translational joints. (c) The orientation of the field-rotation axis at the central point is characterized by the angle of θ and the angle of ϕ . The angle of θ is the one between the projection vector of the field-rotation axis and the positive x-axis, and the angle of ϕ is the one between the vector of the field-rotation axis and the positive z-axis. The range of θ is set as $[0^\circ 360^\circ]$ while the range of ϕ is set as $[0^\circ 180^\circ]$. The largest singular value of Jacobin J_F^+ in θ - ϕ plane, plotted in a logarithmic color scale.

to the angle between the vector of the field-rotation axis and positive z-axis, as shown in Fig 4c. The angle θ is constrained within the range $[0^\circ 360^\circ]$, while ϕ is limited to the range $[67.5^\circ 112.5^\circ]$. These angular constraints define two conical regions corresponding to unreachable motion directions for the TMD, which are symmetric about the xOy plane. It shows the color map of the logarithmic largest singular value of J_F^+ (the abbreviation of $J_F^+(q_n)$) in the θ - ϕ plane at the central point. The color map reveals how hard it is for the field-rotation axis toward the orientation indicated by angles θ and ϕ . As ϕ decreases from 90° to 67.5° or increases from 90° to 112.5° , it gradually becomes harder. Therefore, it indicates that the more vertical the motion direction of a TMD, the more challenging it becomes for the system to implement. In our approach, we adopt a method of having the TMD ascend or descend in a spiral instead of vertically to achieve the TMD's arrival at the designated position.

Characterization of the magnetic field

The two identical magnets, spaced apart by a distance of L_{mag} , are placed symmetrically on the x-axis relative to frame $\{\mathcal{R}\}$ with the unit vector of dipole-rotation axis (Ω) paralleling to the y-axis, as shown in Fig. 5a. The two identical magnets are rotating in synchronization around the dipole-rotation axis (Ω) with a synchronous rotation angle θ_s , resulting in a time-varying magnetic field (magnetic flux density) and field gradient in the workspace of our permanent-magnet robotic system. We study the magnetic field variation within the spherical space centered at the origin and with a radius of r .

Magnetic field strength: the definitions of $\|B\|_{max}$, $\|B\|_{min}$, $\|B\|_{high}$ and $\|B\|_{low}$

For a fixed θ_s and a fixed distance between two actuator magnets (L_{mag}), both maximum and minimum magnetic field strengths ($\|B\|_{max}$ and $\|B\|_{min}$) are present within a specific space. Similarly, for any θ_s with a fixed L_{mag} , both highest and lowest magnetic field strengths ($\|B\|_{high}$ and $\|B\|_{low}$) are also present within the same space. Factors such as the synchronous rotation angle, the distance between two actuator magnets, and joint space variables contribute to a time-varying magnetic field within the workspace of our permanent-magnet robotic system. In this section, we delve into the analysis of the evolving magnetic field and its gradient in the center spherical space resulting from these factors.

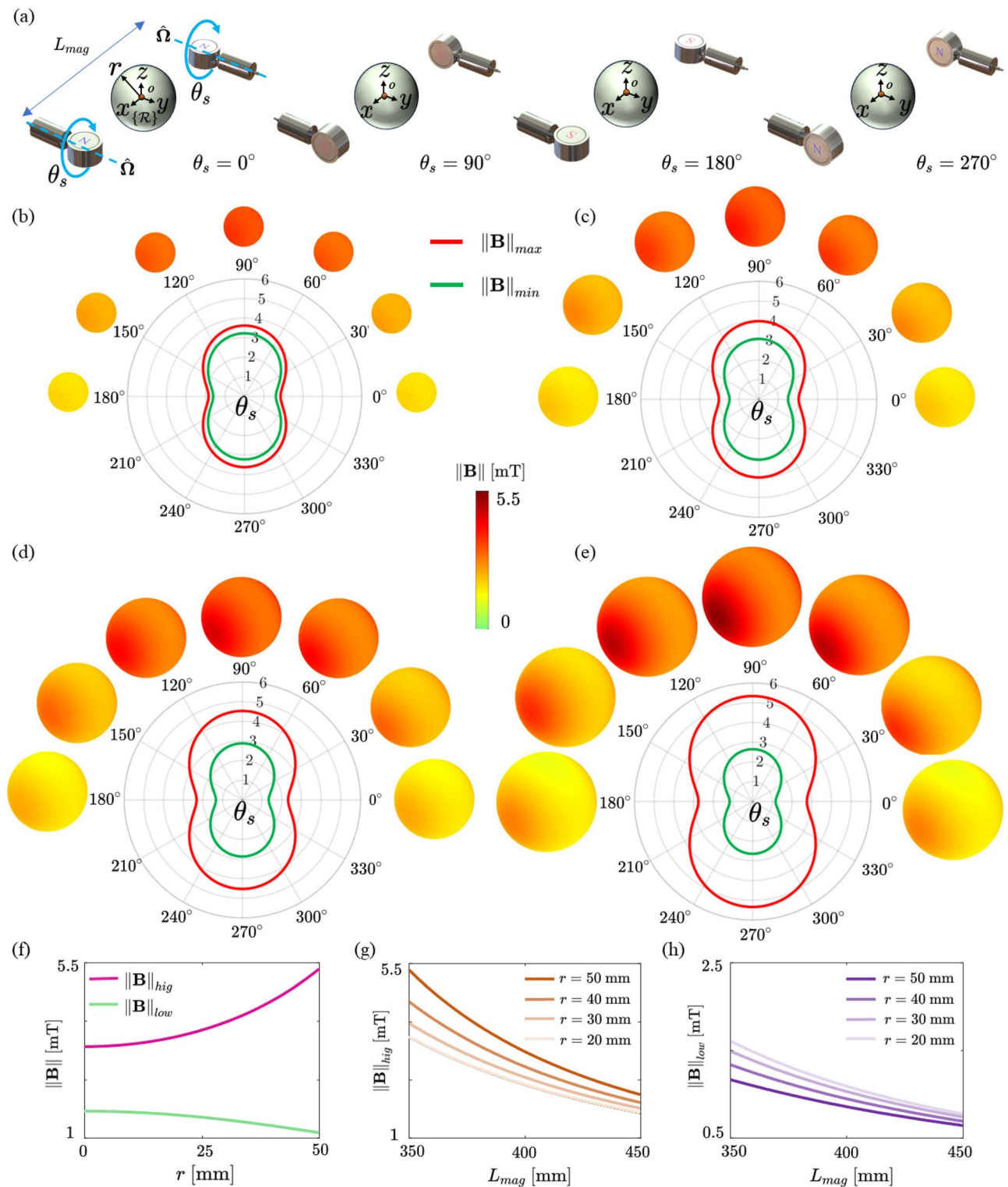


Fig. 5. Two identical magnets are rotated synchronously around the unit vector of dipole-rotation axis $\hat{\Omega}$, resulting in a time-varying magnetic field within the center spherical space. **(a)** Two identical actuator magnets are rotated synchronously around the unit vector of dipole-rotation axis $\hat{\Omega}$. **(b–e)** The maximum and minimum magnetic field strengths ($\|B\|_{max}$ and $\|B\|_{min}$) undergo changes within the center spherical space with a radius of 20 mm, 30 mm, 40 mm, and 50 mm at a constant distance (350 mm) between two actuator magnets during a single rotation period of actuator magnets. The magnetic field strength distribution over the surface of the spherical space varies as θ_s is at several constant degrees (0° , 30° , 60° , 90° , 120° , 150° and 180°). **(f)** The changes of $\|B\|_{high}$ and $\|B\|_{low}$ in relation to the radius of the spherical space at a constant distance (350 mm) between two actuator magnets. **(g,h)** The changes of $\|B\|_{high}$ and $\|B\|_{low}$ at different radii of the center spherical space in relation to the distance (L_{mag}) between two actuator magnets. Please refer to Segment S3 in Supplementary Video.

Synchronous rotation angle

To study the impact of synchronous rotation angle (θ_s) on the magnetic field strength and gradient, we keep the distance between two actuator magnets constant such that $L_{mag} = 350$ mm. As θ_s changes, both the $\|B\|_{max}$ and $\|B\|_{min}$ will vary. This results in the curves showing the changes of $\|B\|_{max}$ and $\|B\|_{min}$, as shown in Fig. 5b–e. The red curve ($\|B\|_{max}$), green curve ($\|B\|_{min}$), and the region between them form a variation band. The variation band becomes wider at a larger center spherical space. The changes of $\|B\|_{max}$ and $\|B\|_{min}$ with respect to θ_s exhibit periodic behavior, with both of them sharing a period of 180° . Furthermore, we visualize the distribution of magnetic field strength over the surface of the central spherical space with radii of 20, 30, 40, and 50 mm, while maintaining θ_s at specific fixed angles (0° , 30° , 60° , 90° , 120° , 150° , and 180°). We observe that the magnetic field strength near the two actuator magnets is greater than in the central region of the sphere.

Radius of the center spherical space

The influence of the radius (r) of the center spherical space on the $\|B\|_{high}$ and $\|B\|_{low}$, with L_{mag} set to 350 mm, is depicted in Fig. 5f. The magnitudes of $\|B\|_{high}$ and $\|B\|_{low}$ at different r are demonstrated in Table 3 (Please refer to Appendix A). As r increases from 0 to 50 mm, the $\|B\|_{high}$ increases from 3.348 to 5.337 mT, whereas the $\|B\|_{low}$ decreases from 1.704 to 1.167 mT, indicating that the rate at which the $\|B\|_{high}$ increases is faster than the rate at which the $\|B\|_{low}$ decreases.

Distance between two actuator magnets

The influence of the distance (L_{mag}) between two actuator magnets on the $\|B\|_{high}$ and $\|B\|_{low}$ are shown in Fig. 5g,h, respectively. As L_{mag} increases, $\|B\|_{high}$ decreases at a faster rate compared to $\|B\|_{low}$. Further, the $\|B\|_{high}$ at a larger r decreases faster while $\|B\|_{low}$ at a smaller r decreases faster. Specifically, as L_{mag} increases from 350 to 450 mm, the $\|B\|_{high}$ at $r = 20, 30, 40$ and 50 mm decreases from 3.615 to 1.658 mT, 3.973 to 1.757 mT, 4.526 to 1.904 mT and 5.337 to 2.108 mT, respectively. The $\|B\|_{low}$ at $r = 20, 30, 40$ and 50 mm decreases from 1.605 to 0.771 mT, 1.489 to 0.737 mT, 1.340 to 0.692 mT and 1.167 to 0.638 mT, respectively.

Magnetic field gradient: the definitions of $\|\nabla B\|_{max}$, $\|\nabla B\|_{min}$, $\|\nabla B\|_{high}$ and $\|\nabla B\|_{low}$

Similar to the definition in magnetic field strength, for a fixed θ_s and a fixed distance between two actuator magnets (L_{mag}), both maximum and minimum magnetic field gradients ($\|\nabla B\|_{max}$ and $\|\nabla B\|_{min}$) are present within a specific space. Comparatively, for any θ_s with a fixed L_{mag} , both highest and lowest magnetic field gradients ($\|\nabla B\|_{high}$ and $\|B\|_{low}$) are also present within the same space.

Synchronous rotation angle

The change of maximum field gradient $\|\nabla B\|_{max}$ along with the synchronous rotation angle (θ_s) is periodic with a period of 180° , as shown in Fig. 6a–d. Besides, the magnetic field gradient distribution over the surface of the center spherical space with the radius of 20, 30, 40, and 50 mm while keeping θ_s at a set of constant degrees (0° , 30° , 60° , 90° , 120° , 150° and 180°) is visualized. It is evident that the magnetic field gradient is noticeably higher in the vicinity of the actuator magnets within the spherical space compared to the central portion of the sphere.

Radius of the center spherical space

With an increasing radius (r) of the center spherical space, $\|\nabla B\|_{max}$ also exhibits a corresponding increase. Note that the minimum field gradient $\|\nabla B\|_{min}$ is equal to 0 for any θ_s . As r increases from 0 to 50 mm, $\|\nabla B\|_{high}$ increases from 0 to 0.097 T/m, as shown in Fig. 6e. Note that the $\|\nabla B\|_{low}$ remains to be 0.

Distance between two actuator magnets

The influence of L_{mag} on the $\|\nabla B\|_{high}$ is shown in Fig. 6f. As L_{mag} increases, $\|\nabla B\|_{high}$ at a larger r decreases faster. Specifically, as L_{mag} increases from 350 to 450 mm, the $\|\nabla B\|_{high}$ at $r = 20, 30, 40$ and 50 mm decreases from 0.028 to 0.008 T/m, 0.045 to 0.012 T/m, 0.067 to 0.017 T/m and 0.097 to 0.024 T/m, respectively.

Free-gradient region

A space is assumed to be a gradient-free if the magnitude of magnetic field gradient within the space below a threshold (ϱ) such that $\|\nabla B\|_{high} \leq \varrho$. The threshold determines the degree of gradient-free in that space. The smaller the threshold, the higher the degree of gradient-free in the space. As L_{mag} increases, the radius (r_g) of the gradient-free space expands for a set of given thresholds, as shown in Fig. 6g. Specifically, as L_{mag} increases from 350 to 450 mm, the r_g at $\varrho = 0.005, 0.01, 0.015$ and 0.02 increases from 3.86 to 13.23 mm, 7.67 to 25.29 mm, 11.38 to 35.65 mm, and 14.95 to 44.36 mm, respectively. Conversely, the desired distance (L_{mag}^d) between two actuator magnets can be calculated for the gradient-free space with a required size at a specified threshold. The size of the gradient-free space can be enlarged by increasing the distance between the two actuator magnets. However, this comes at the expense of the average magnetic field strength in the gradient-free space.

In addition, the motion of each robotic joint influences the distribution of both the magnetic field strength and the field gradient within the central spherical region. Visualizations illustrating how each joint's motion affects the magnetic field strength and the field gradient are provided in Segments S5 and S6 of the Supplementary Video, respectively.

Closed-loop motion control

A TMD is controlled to follow three predefined 2-D trajectories and a 3-D spiral circular trajectory in an agar-gel tissue phantom to verify the capability of our permanent magnet-robotic system of implementing TMD motion control. The TMD consists of a twist body and a cylindrical magnet. The body of the TMD is fabricated using a

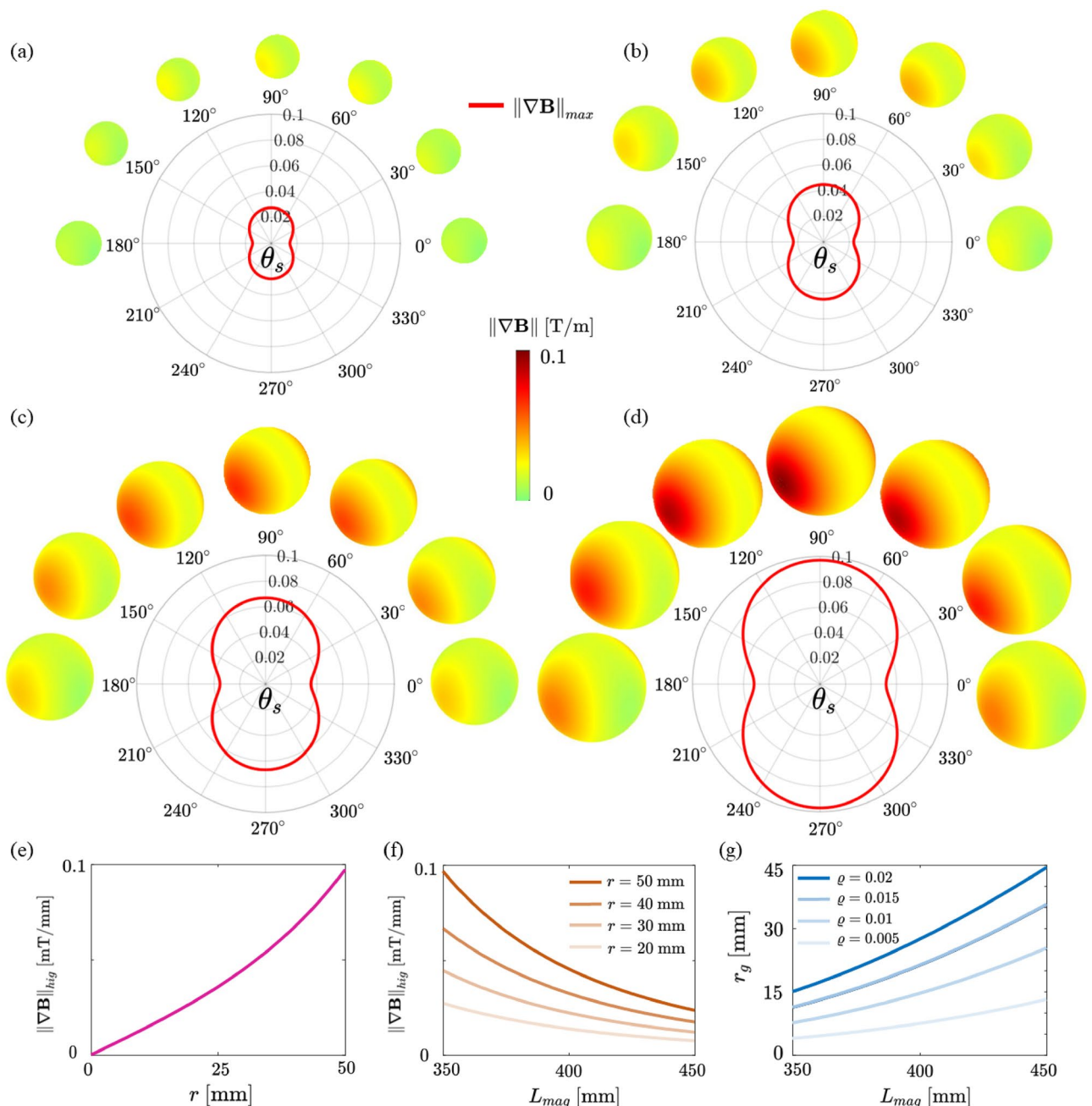


Fig. 6. The result of varying magnetic field gradients on the center spherical space between two actuator magnets. (a–d) The maximum magnetic field gradient changes within the center spherical space with a radius of 20 mm, 30 mm, 40 mm, and 50 mm at a distance (350 mm) between two actuator magnets during a single rotation period of actuator magnets. The magnetic field gradient distribution over the surface of the spherical space with a radius of 20 mm, 30 mm, 40 mm, and 50 mm varies as θ_s is at different degrees (0°, 30°, 60°, 90°, 120°, 150° and 180°). (e) The change of the $\|\nabla B\|_{\text{high}}$ in relation to the radius (r) of the spherical space at a constant distance (350 mm) between two actuator magnets. (f) The change of $\|\nabla B\|_{\text{high}}$ in response to the distance (L_{mag}) between two actuator magnets. (g) The change of the radius (r_g) of gradient-free space in response to L_{mag} for a set of given thresholds (ρ). Please refer to Segment S4 in Supplementary Video.

3D printer with Formlabs photopolymer resin (FLGPBK04), and has a length of 4 mm, a diameter of 1.5 mm, and a weight of 0.0049 g. The magnet of the TMD is made of Grade-N45 NdFeB and axially magnetized with the diameter of 1 mm and the height of 1 mm, and it has the weight of 0.0064 gram. The magnet is positioned at the tail with its dipole moment being perpendicular to the helix axis of the TMD. The two identical actuator magnets are fabricated with cylindrical Grade-N45 NdFeB and axially magnetized. Each of them has the diameter of 45 mm and the height of 30 mm. Further, the actuator magnets are controlled to rotate synchronously. Each of

them is driven by a Maxon motor (Planetary Gearhead GP 32 C D32 mm, 1.0–6.0 Nm, Ceramic Version) with a Maxon controller (EPOS2 50/5, Digital positioning controller, 5 A, 11–50 VDC).

The field-rotation axis's translational motion, characterized by joint space variable q_1 , is implemented by a linear motion stage (KUA1505-520-150-A1-N3, X-Axis unit, Japan). Further, the motion stage is driven by an A1 actuator (MX-106R, Dynamixel Actuator). The yawing motion of the field-rotation axis, which is characterized by joint space variable q_2 , is accomplished by an A2 actuator (H42P-020-S300-R, Servomoteur Dynamixel PRO PLUS). The pitching motion of the field-rotation axis, which is characterized by joint space variable q_3 , is realized by two A1 actuators which are in synchronous control mode. Another yawing motion of the field-rotation axis, characterized by joint space variable q_4 , is fulfilled by two A3 actuators (M42P-010-S260-R, Servomoteur Dynamixel PRO PLUS).

To measure the real-time position and the moving direction of the TMD, two cameras (Aviator GIGE, avA1000-100gm, Basler AG, Ahrensburg, Germany) are mounted on orthogonal sides of the container. Besides, the TMD is immersed in agar-gel tissue phantom which is made of gelatine powder (Ec Nr: 232-554-6, Boom BV, Rabroekenweg, The Netherlands) and demineralized water with a mass ratio of 0.63 wt%. To make the agar-gel tissue phantom, we put the aqueous solution of which inside a transparent cubical container with a length of 100 mm, and afterward the aqueous solution is stored in a refrigerator at a temperature of 4 degrees Celsius for 12 hours prior to the experiment. The TMD is actuated under the actuation frequency of 2 Hz during the closed-loop motion control.

Two-dimensional motion control

We implement 2-D closed-loop motion control experiments with two prescribed trajectories. To begin with, the prescribed “Triangle” and “Square” trajectories are broken into 32 and 18 representative waypoints, respectively. Then, the desired inverse solution at each representative point of prescribed trajectories is solved based on the algorithm presented in Algorithm 1. Next, these inverse solutions provide the real-time reference positions for joint space variables during the implementations of TMD closed-loop motion control. The prescribed (red) and actual (blue) trajectories with their tracking errors are indicated in each case, as shown in Fig. 7. It indicates that the maximum position tracking errors of the “Triangle” and “Square” trajectories are 1.94 mm and 1.20 mm, respectively. The increase in the motion speed of the TMD can be achieved by increasing the actuation frequency. However, increasing the TMD's motion speed requires the system to have the capability to respond quickly. Otherwise, it may lead to an increase in position tracking error. Please refer to Segment S7 in [Supplementary Video](#).

Three-dimensional motion control

We implement 3-D closed-loop motion control experiments with one prescribed trajectory. To begin with, the prescribed 3-D spiral trajectory is broken into 17 representative waypoints (see Table 1). These waypoints are evenly distributed on the predefined trajectory. The desired field-rotation axis at each representative waypoint is indicated by red arrow. Given the representative waypoint P_n and the desired field-rotation axis $\hat{\omega}^d$, the desired dipole-rotation axis $\hat{\Omega}^d$, and the desired vector of joint space variables q^d at each waypoint is calculated in Table 1 by using the algorithm presented in Algorithm 1.

The time-dependent changes of reference (red) and actual (blue) positions in joint space variables are shown in Fig. 8a. The time-dependent change of q_1 shows a tendency for the linear motion stage to move forth and

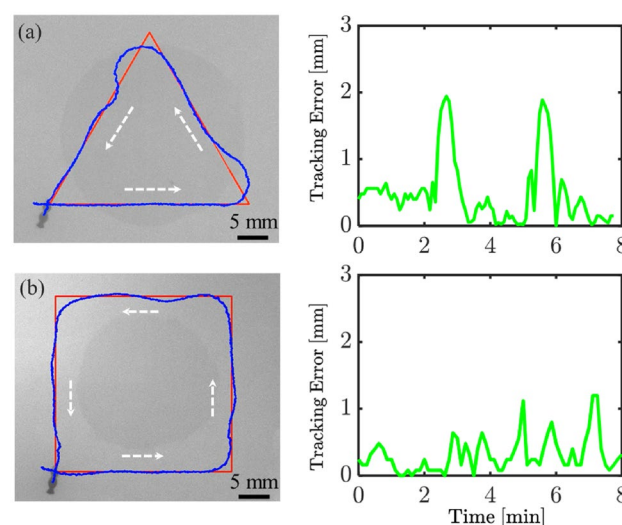


Fig. 7. 2-D closed-loop motion control of a TMD to move along a prescribed 2-D trajectories. (a) “Triangle” trajectory with its tracking error. (b) “Square” trajectory with its tracking error. The prescribed trajectories (red) and the actual trajectories (blue) are indicated. The TMD achieves an average motion speed of 0.27 mm/s during the closed-loop motion control. Please refer to Segment S7 in [Supplementary Video](#).

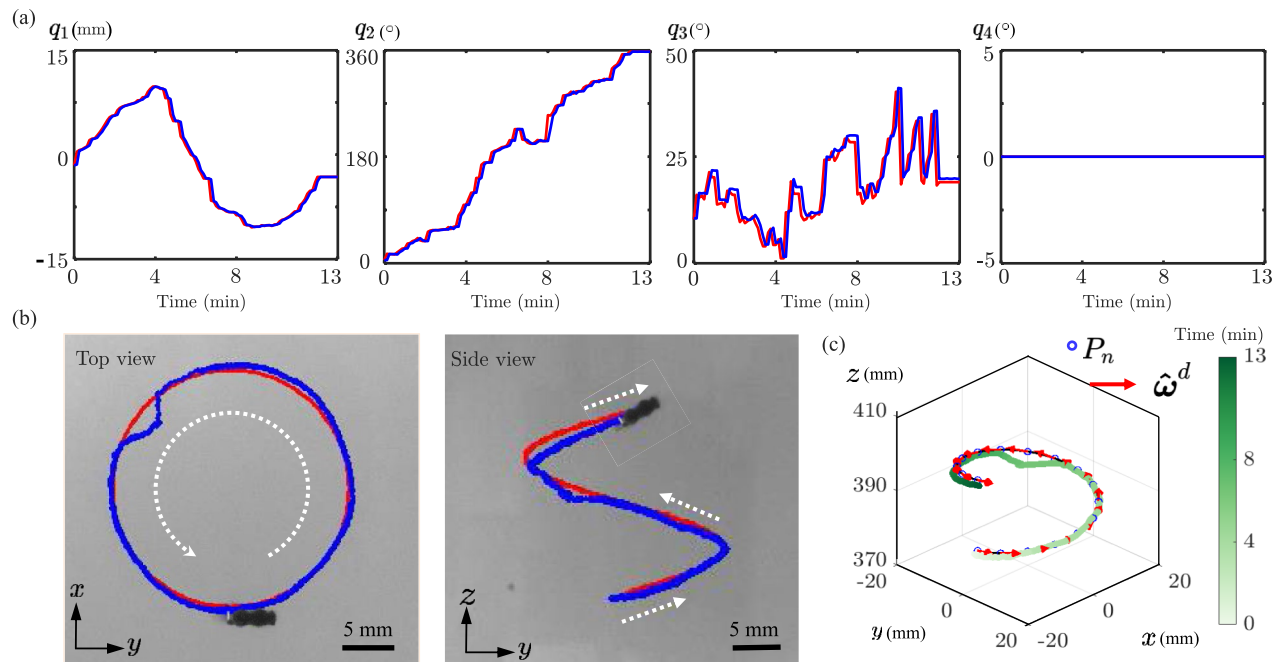


Fig. 8. 3-D closed-loop motion control of a TMD is implemented using our permanent magnet-based robotic system. The TMD is controlled to follow a predefined 3-D spiral trajectory inside a square container (with the side length of 100 mm) filled with agar-gel tissue phantom. **(a)** The reference position (red) and actual position (blue) of each joint variable indicates the control input and output of each joint variable. **(b)** The actual track points from the top view form a circle with a diameter of 30.6 mm, and those in the side view form the rising spirals with a pitch of 19.0 mm. **(c)** The synthetic 3-D trajectory (green) indicates the mean absolute error compared to the predefined one (black) is 1.18 mm and the maximum tracking error is 2.64 mm. The desired field-rotation axis at each representative point is indicated by a red arrow. Please refer to Segment S8 in [Supplementary Video](#).

back to follow the TMD motion in the y -axis direction. The time-dependent change of q_2 indicates that the bottom yawing motor approximately rotates 22° at two adjacent representative waypoints. The time-dependent change of q_3 indicates that the pitching motor decreases its pitching angle as the TMD moves upward. The time-dependent change of q_4 indicates that the two top yawing motors make a small rotation. As we look at the time-dependent changing trend of each joint space variable, the control system tends to keep the TMD at the center of the workspace throughout the process of controlling the TMD to move along the predefined trajectories.

Figure 8b indicates the real-time position of the TMD at the top and side views. From the top view, the TMD trajectory forms a circle with a diameter of 30.6 mm. From the side view, the trajectory forms a spiral with a pitch of 19.0 mm. Further, Fig. 8c demonstrates that the mean absolute error of 3-D motion control, by calculating the average positioning error between the synthetic and predefined 3-D trajectory (green and black), is 1.18 mm, and the maximum tracking error is 2.64 mm. Experimental results reveal that the TMD can move controllably. Please refer to Segment S8 in [Supplementary Video](#).

Conclusion

We develop a permanent magnet-based robotic system which enables motion control of TMDs. First, we derive a kinematic model which relates the field-rotation axis, the dipole-rotation axis and the joint space variables. Then, we characterize the yawing and pitching motion of the field-rotation axis at the central point of workspace. Next, we analyze the difficulty level of orienting the field-rotation axis at the central point of the workspace and observe that the system exhibits greater degree of singularity as the field-rotation axis becomes vertical. Then, we characterize the magnetic field and field gradient in workspace and observe that the center region of the workspace is almost a gradient-free region. Finally, we demonstrate the capability of our robotic system to control a TMD moving along prescribed trajectories in 2-D and 3-D space experimentally. In addition, our system is not only capable of driving highly magnetized devices, like those containing NdFeB magnets for magnetization, but also caters to weakly magnetized devices, such as soft sperm robots that utilize injected magnetic particles for magnetization^{42,43}.

Data Availability

The datasets generated during this study include experimental and simulation videos, which are provided as supplementary material.

Appendix 1

Frame parameters of the permanent-magnet based robotic system

The parameters corresponding to each frame shown in Fig. 2 are demonstrated in Table 2 as below. In which, for $i = 1$, $d_x^4 = l_5$ and $d_y^4 = -l_6$, and for $i = 2$, $d_x^4 = -l_5$ and $d_y^4 = l_6$.

j	q_j	d_x^j	d_y^j	d_z^j	q_{\min}	q_{\max}
1	q_1 [mm]	–	–	–	–150	150
2	q_2 [°]	–	–	l_2	–720	720
3	q_3 [°]	–	–	l_3	–90	90
4	q_4 [°]	$\pm l_5$	$\mp l_6$	l_4	–180	180

Table 2. Frame parameters of the robotic system.

r [mm]	20	30	40	50
$\ B\ _{high}$ [mT]	3.615	3.973	4.526	5.337
$\ B\ _{low}$ [mT]	1.605	1.489	1.340	1.167
$\ \nabla B\ _{high}$ [T/m]	0.028	0.045	0.067	0.097
$\ \nabla B\ _{low}$ [T/m]	0	0	0	0

Table 3. Characterization of magnetic filed.

Appendix 2

Characterization of magnetic filed

Highest and lowest magnetic field strengths, and highest field gradient within the center spherical space of different radii within a rotation period of actuator magnets.

Received: 23 May 2025; Accepted: 6 August 2025

Published online: 23 August 2025

References

- Nelson, B. J., Kaliakatsos, I. K. & Abbott, J. J. Microrobots for minimally invasive medicine. *Annu. Rev. Biomed. Eng.* **12**, 55–85 (2010).
- Jang, D., Jeong, J., Song, H. & Chung, S. K. Targeted drug delivery technology using untethered microrobots: A review. *J. Micromech. Microeng.* **29**(5), 053002 (2019).
- Cai, Z. et al. Performance evaluation of a magnetically driven microrobot for targeted drug delivery. *Micromachines* **12**(10), 1210 (2021).
- Yang, L., Wang, Q. & Zhang, L. Model-free trajectory tracking control of two-particle magnetic microrobot. *IEEE Trans. Nanotechnol.* **17**(4), 697–700 (2018).
- Ricotti, L. & Menciassi, A. Nanotechnology in biorobotics: Opportunities and challenges. *J. Nanopart. Res.* **17**(2), 1–10 (2015).
- Wang, Y. et al. A microfluidic robot for rare cell sorting based on machine vision identification and multi-step sorting strategy. *Talanta* **226**, 122136 (2021).
- Wang, J.-W. et al. Miniaturization of the whole process of protein crystallographic analysis by a microfluidic droplet robot: From nanoliter-scale purified proteins to diffraction-quality crystals. *Anal. Chem.* **91**(15), 132–140 (2019).
- Khalil, I. S. et al. Mechanical rubbing of blood clots using helical robots under ultrasound guidance. *IEEE Robot. Autom. Lett.* **3**(2), 1112–1119 (2018).
- Mahdy, D., Reda, R., Hamdi, N. & Khalil, I. S. Ultrasound-guided minimally invasive grinding for clearing blood clots: Promises and challenges. *IEEE Instrum. Meas. Mag.* **21**(2), 10–14 (2018).
- Oulmas, A., Andreff, N. & Régnier, S. 3d closed-loop motion control of swimmer with flexible flagella at low reynolds numbers, In *2017 IEEE/RSJ International Conference on Intelligent Robots and Systems (IROS)* 1877–1882 (IEEE, 2017).
- Xu, T., Hwang, G., Andreff, N. & Régnier, S. Planar path following of 3-d steering scaled-up helical microswimmers. *IEEE Trans. Rob.* **31**(1), 117–127 (2015).
- Oulmas, A., Andreff, N. & Régnier, S. Chained formulation of 3d path following for nonholonomic autonomous robots in a Serret–Frenet frame. In *2016 American Control Conference (ACC)* 7275–7280 (IEEE, 2016).
- Park, C., Kim, J., Kim, S.-J. & Yoo, J. Development of a permanent magnet type micro-robot actuated by external electromagnetic system. *Microsyst. Technol.* **21**(6), 1257–1265 (2015).
- Khalil, I. S., Abelman, L. & Misra, S. Magnetic-based motion control of paramagnetic microparticles with disturbance compensation. *IEEE Trans. Magn.* **50**(10), 1–10 (2014).
- Ongaro, F., Pane, S., Scheggi, S. & Misra, S. Design of an electromagnetic setup for independent three-dimensional control of pairs of identical and nonidentical microrobots. *IEEE Trans. Rob.* **35**(1), 174–183 (2018).
- Zheng, L. et al. 3d navigation control of untethered magnetic microrobot in centimeter-scale workspace based on field-of-view tracking scheme. *IEEE Trans. Robot.* **1**, 1 (2021).

17. Zhong, S. et al. Spatial constraint-based navigation and emergency replanning adaptive control for magnetic helical microrobots in dynamic environments. *IEEE Trans. Autom. Sci. Eng.* **21**(4), 7180–7189 (2024).
18. Wang, H. et al. Data-driven parallel adaptive control for magnetic helical microrobots with derivative structure in uncertain environments. *IEEE Trans. Syst. Man Cybern. Syst.* **54**(7), 4139–4150 (2024).
19. Zhong, S. et al. Paired interactions of magnetic millirobots in confined spaces through data-driven disturbance rejection control under global input. In *IEEE/ASME Transactions on Mechatronics* 1–12 (2025).
20. Janssen, H., Ter Maten, E. & Van Houwelingen, D. Simulation of coupled electromagnetic and heat dissipation problems. *IEEE Trans. Magn.* **30**(5), 3331–3334 (1994).
21. Erni, S., Schürle, S., Fakhraee, A., Kratochvil, B. E. & Nelson, B. J. Comparison, optimization, and limitations of magnetic manipulation systems. *J. Micro-Bio Robot.* **8**(3), 107–120 (2013).
22. Fountain, T. W., Kailat, P. V. & Abbott, J. J. Wireless control of magnetic helical microrobots using a rotating-permanent-magnet manipulator. In *2010 IEEE International Conference on Robotics and Automation* 576–581 (IEEE, 2010).
23. Mahoney, A. W. & Abbott, J. J. Generating rotating magnetic fields with a single permanent magnet for propulsion of untethered magnetic devices in a lumen. *IEEE Trans. Robot.* **30**(2), 411–420 (2013).
24. Nelson, N. D. & Abbott, J. J. Generating two independent rotating magnetic fields with a single magnetic dipole for the propulsion of untethered magnetic devices. In *2015 IEEE International Conference on Robotics and Automation (ICRA)* 4056–4061 (IEEE, 2015).
25. Mahoney, A. W., Wright, S. E. & Abbott, J. J. Managing the attractive magnetic force between an untethered magnetically actuated tool and a rotating permanent magnet. In *2013 IEEE International Conference on Robotics and Automation* 5366–5371 (IEEE, 2013).
26. Hosney, A., Klingner, A., Misra, S. & Khalil, I. S. Propulsion and steering of helical magnetic microrobots using two synchronized rotating dipole fields in three-dimensional space. In *2015 IEEE/RSJ International Conference on Intelligent Robots and Systems (IROS)* 1988–1993 (IEEE, 2015).
27. Zhang, W., Meng, Y. & Huang, P. A novel method of arraying permanent magnets circumferentially to generate a rotation magnetic field. *IEEE Trans. Magn.* **44**(10), 2367–2372 (2008).
28. Qiu, T., Palagi, S., Sachs, J. & Fischer, P. Soft miniaturized linear actuators wirelessly powered by rotating permanent magnets. In *2018 IEEE International Conference on Robotics and Automation (ICRA)* 3595–3600 (IEEE, 2018).
29. Khalil, I. S. et al. Positioning of drug carriers using permanent magnet-based robotic system in three-dimensional space. In *2017 IEEE International Conference on Advanced Intelligent Mechatronics (AIM)* 1117–1122 (IEEE, 2017).
30. Mahoney, A. W. & Abbott, J. J. Five-degree-of-freedom manipulation of an untethered magnetic device in fluid using a single permanent magnet with application in stomach capsule endoscopy. *Int. J. Robot. Res.* **35**(1–3), 129–147 (2016).
31. Shapiro, B., Dormer, K. & Rutel, I. B. A two-magnet system to push therapeutic nanoparticles. *AIP Conf. Proc.* **1311**, 77 (2010).
32. Amokrane, W., Belharet, K. & Ferreira, A. Design and modeling of a two-magnet actuator for robotic micromanipulation. *Sens. Actuators A* **316**, 112391 (2020).
33. Abbes, M., Belharet, K., Mekki, H. & Poisson, G. Permanent magnets based actuator for microrobots navigation. In *2019 IEEE/RSJ International Conference on Intelligent Robots and Systems (IROS)* 7062–7067 (IEEE, 2019).
34. Son, D., Ugurlu, M. C. & Sitti, M. Permanent magnet array-driven navigation of wireless millirobots inside soft tissues. *Sci. Adv.* **7**(43), eabi8932 (2021).
35. Mahoney, A. W. & Abbott, J. J. Managing magnetic force applied to a magnetic device by a rotating dipole field. *Appl. Phys. Lett.* **99**(13), 134103 (2011).
36. Hosney, A., Abdalla, J., Amin, I. S., Hamdi, N. & Khalil, I. S. In vitro validation of clearing clogged vessels using microrobots. In *2016 6th IEEE International Conference on Biomedical Robotics and Biomechanics (BioRob)* 272–277 (IEEE, 2016).
37. Pittiglio, G. et al. Collaborative magnetic manipulation via two robotically actuated permanent magnets. *IEEE Trans. Robot.* **1**, 1 (2022).
38. Ryan, P. & Diller, E. Magnetic actuation for full dexterity microrobotic control using rotating permanent magnets. *IEEE Trans. Robot.* **33**(6), 1398–1409 (2017).
39. Carpi, F. & Pappone, C. Stereotaxis niobe® magnetic navigation system for endocardial catheter ablation and gastrointestinal capsule endoscopy. *Expert Rev. Med. Devices* **6**(5), 487–498 (2009).
40. Caciagli, A., Baars, R. J., Philipse, A. P. & Kuipers, B. W. Exact expression for the magnetic field of a finite cylinder with arbitrary uniform magnetization. *J. Magn. Magn. Mater.* **456**, 423–432 (2018).
41. Mahoney, A. W. & Abbott, J. J. 5-dof manipulation of an untethered magnetic device in fluid using a single permanent magnet. In *Robotics: Science and Systems* (2014).
42. Magdanz, V. et al. Ironsperm: Sperm-templated soft magnetic microrobots. *Sci. Adv.* **6**(28), eaba5855 (2020).
43. Wang, Z., Klingner, A., Magdanz, V., Misra, S. & Khalil, I. S. Soft bio-microrobots: Toward biomedical applications. *Adv. Intell. Syst.* **1**, 2300093 (2023).

Acknowledgements

The authors would like to thank E.D. de Jong and Mert Kaya for fabricating mechanical parts during the development of our permanent-based robotic system, and thank Zihan Wang for providing the assistance of image tracking of tetherless magnetic devices.

Author contributions

I.S.M.K. contributed to the conception and overall design of the study. Z.Z. conducted the experiments, contributed to the methodology, and wrote the manuscript. S.M. supervised the project and provided methodological analysis. A.K. proposed the initial idea and provided critical comments on the manuscript. All authors reviewed and approved the final version of the manuscript.

Funding

This work is supported in part by the European Research Council (ERC) under the European Unions Horizon 2020 Research, in part by Innovation programme under Grant 866494 project-MAESTRO, and in part by the financial support from the China Scholarship Council.

Declarations

Competing interests

The authors declare no competing interests.

Additional information

Supplementary Information The online version contains supplementary material available at <https://doi.org/10.1038/s41598-025-15247-7>.

Correspondence and requests for materials should be addressed to I.S.M.K.

Reprints and permissions information is available at www.nature.com/reprints.

Publisher's note Springer Nature remains neutral with regard to jurisdictional claims in published maps and institutional affiliations.

Open Access This article is licensed under a Creative Commons Attribution-NonCommercial-NoDerivatives 4.0 International License, which permits any non-commercial use, sharing, distribution and reproduction in any medium or format, as long as you give appropriate credit to the original author(s) and the source, provide a link to the Creative Commons licence, and indicate if you modified the licensed material. You do not have permission under this licence to share adapted material derived from this article or parts of it. The images or other third party material in this article are included in the article's Creative Commons licence, unless indicated otherwise in a credit line to the material. If material is not included in the article's Creative Commons licence and your intended use is not permitted by statutory regulation or exceeds the permitted use, you will need to obtain permission directly from the copyright holder. To view a copy of this licence, visit <http://creativecommons.org/licenses/by-nc-nd/4.0/>.

© The Author(s) 2025